IAC-23-A6.1.3

# Effects of Phase Angle and Sensor Properties on On-Orbit Debris Detection Using Commercial Star Trackers

**Allan Shtofenmakher**[a,*], **Hamsa Balakrishnan**[b]

[a] *Ph.D. Candidate, Department of Aeronautics and Astronautics, Massachusetts Institute of Technology, Cambridge, MA 02139, USA, ashtofen@mit.edu*

[b] *William E. Leonhard (1940) Professor, Department of Aeronautics and Astronautics, Massachusetts Institute of Technology, Cambridge, MA 02139, USA, hamsa@mit.edu*

[*] Corresponding Author

## Abstract

The recent proliferation of resident space objects (RSOs) in low Earth orbit (LEO) threatens the sustainability of space as a resource and requires persistent monitoring to avoid collisions involving valuable space assets. State-of-the-art ground-based space surveillance techniques, due to their susceptibility to atmosphere, weather, and lighting conditions, tend to focus on RSOs with characteristic length greater than 10 cm or 1 dm. Consequently, millions of smaller LEO RSOs remain untracked by ground-based methods, which reduces overall space situational awareness. Onboard satellite sensors offer a space-based method for tracking RSOs. Prior research has investigated the feasibility of using commercial star trackers (CSTs)—optical sensors prevalent on most active spacecraft—to observe, detect, and estimate the position and velocity of RSOs larger than 10 cm. In a recent effort, we expanded on these feasibility studies by assessing the capabilities of CSTs to detect debris particles smaller than 10 cm in characteristic length. We modeled the particles as Lambertian spheres with zero phase angle and ten percent reflectivity and found that typical CSTs can detect properly illuminated debris of characteristic length between 1 cm and 10 cm even at distances of tens of kilometers. More sensitive CSTs can characterize decimeter-scale RSOs hundreds of kilometers away; alternatively, they can track centimeter-scale and smaller RSOs at closer distances. In this paper, we summarize these key results and extend our previous study by relaxing its zero-phase-angle assumption and characterizing the effect of Sun-RSO-CST phase angle on debris detection range. We identify a number of representative CSTs with publicly available optical characteristics and consider the effects of properties such as pixel pitch, focal length, aperture diameter, and field of view (FOV) on the capability of each CST to detect debris at a given distance and relative velocity (in the form of streak speed). We find that, for debris particles modeled as diffuse Lambertian spheres, Sun-RSO-CST phase angles as high as 57° result in no more than 20% reduction to the useful RSO-CST detection range. In addition, we find that pixel pitch and focal length, rather than aperture diameter, tend to determine the capability of a given CST to resolve two distinct RSOs. Furthermore, streak speed may serve as a stronger limiting factor for detection of smaller debris particles than for larger ones. Despite these limitations, the overall results indicate that CSTs have the potential to substantially enhance space-based debris detection capability.

**Keywords:** Space Situational Awareness (SSA); Space-Based Space Surveillance; Orbital Debris Detection; Space-Based Optical Sensors; Small Orbital Debris; Apparent Visual Brightness

## Nomenclature

| | |
|---|---|
| $A_{\mathrm{opt}}$ | Optical Cross Section |
| $d$ | Debris Diameter or Characteristic Length |
| $D$ | Aperture Diameter |
| $f$ | Focal Length |
| $F(\phi)$ | Phase Function |
| $M$ | Pixel Count (One Side of Square Frame) |
| $p$ | Pixel Pitch |
| $R$ | RSO-CST Distance or Range |
| $S_{\mathrm{max}}$ | Maximum Streak Speed |
| $V_{\mathrm{cutoff}}$ | AVM Cutoff of CST |
| $V_{\mathrm{rso}}$ | AVM of RSO |
| $V_{\mathrm{sun}}$ | AVM of Sun |
| $\theta_{\mathrm{p}}$ | Pixel FOV (One Side of Square Frame) |
| $\theta_{\mathrm{R}}$ | Rayleigh Criterion |
| $\lambda$ | Wavelength (of Light) |
| $\rho$ | Reflectivity |
| $\tau$ | Exposure Time |
| $\phi$ | Phase Angle |
| $\psi$ | Sensor FOV (One Side of Square Frame) |

## Acronyms

| | |
|---|---|
| AVM | Apparent Visual Magnitude |
| BST | Berlin Space Technologies |
| CST | Commercial Star Tracker |
| FI | Front-Illuminated (CST) |
| FOV | Field of View |
| GRD | Ground Resolution Distance |
| HP | High-Precision (CST) |
| IADC | Inter-Agency Space Debris Coordination Committee |
| LEO | Low Earth Orbit |
| OCS | Optical Cross Section |
| PSRD | Projected Space Resolution Distance |
| PSSD | Projected Space Sample Distance |
| RSO | Resident Space Object |
| SNR | Signal-to-Noise Ratio |
| SSA | Space Situational Awareness |
| SSN | Space Surveillance Network |
| ST | Star Tracker |
| STEM | Science, Tech., Engineering, and Math. |

## 1. Introduction and Background

The recent proliferation of resident space objects (RSOs) in low Earth orbit (LEO) threatens the sustainability of space as a resource and requires persistent monitoring to avoid collisions involving valuable space assets [1]. Over 23,000 LEO RSOs—including active satellites, inactive satellites, and non-functional debris—are currently tracked by the U.S. Space Surveillance Network (SSN) [2]. The SSN relies primarily on ground-based space surveillance equipment, such as radar and optical telescopes, which are susceptible to atmosphere, weather, and lighting conditions [3], [4]. These barriers generally limit the focus of state-of-the-art space surveillance methods to RSOs with characteristic length greater than 10 cm or 1 dm, leaving millions of LEO RSOs smaller than 10 cm untracked and uncatalogued [2].

The reduced space situational awareness (SSA) in this regime has had expensive consequences. In December 2022, the Soyuz MS-22 module attached to the International Space Station suffered a coolant leak that rendered the vehicle unsafe to complete its intended mission of returning its crew back to Earth [5]. Instead, the Soyuz MS-23 module had to be commissioned to replace its damaged counterpart at an estimated launch cost of $80M [5], [6]. This leak is suspected to have been caused by an RSO approximately 1 mm in characteristic length [7].

Reducing the risk of further space asset compromise is a priority that requires improved space debris detection and tracking capabilities. Space-based sensors offer a potential solution to this problem. Unlike their ground-based counterparts, they are generally unaffected by atmosphere, weather, and lighting conditions. Moreover, they tend to be more sensitive and, consequently, can detect smaller and dimmer RSOs [4]. The Space-Based Visible sensor onboard the Midcourse Space Experiment satellite first demonstrated the potential of using onboard satellite sensors to detect and track RSOs in 1998 [8]. Since then, space-based space surveillance has been integral to the SSN's mission, with additional space-based assets deployed every few years [3], [9]. However, the recent, dramatic proliferation of RSOs in LEO, especially when compared to the slow rate of growth in the number of dedicated SSN assets, indicates the need for a far more scalable, widespread, and—ideally—low-cost solution [3]. One promising approach involves the commercial star tracker (CST), an optical sensor used by satellites to determine spacecraft attitude by capturing images of distant stars and comparing them to onboard star catalogs [10]. In addition to stars, these images also often capture incidental RSOs that are within line of sight of the CST and are adequately illuminated by the Sun [10]. The positions and velocities of these RSOs can be estimated using a variety of machine learning algorithms, often involving convolutional neural networks and models for characterizing image streak patterns [11], [12], [13], [14].

Since the vast majority of currently active satellites feature at least one CST, recent research has investigated the potential for leveraging the thousands of commercial star trackers already on orbit as part of a near-zero-cost distributed space surveillance system [4], [10], [11], [12], [15], [16]. Various noteworthy endeavors include: assessing the effectiveness of observing and detecting RSOs in simulated CST images [15]; exploring methods for estimating the positions and velocities of such RSOs [11], [12]; and developing methods for increasing the accuracy of RSO orbit estimates using multiple CSTs distributed across space and time [10]. However, the majority of these efforts has focused on improving state estimates for those RSOs that are already tracked by the SSN—that is, those with characteristic length larger than 10 cm, in general.

Recently, we have begun investigating the potential for using CSTs to detect and track debris particles *smaller than* 10 cm. We explored the relationship among the apparent visual magnitude (AVM) of the RSO—or the apparent brightness of the RSO as perceived by the observing CST—RSO size, and RSO-CST distance, establishing a parameter space (in terms of the latter two parameters) within which a given CST can feasibly detect debris particles in LEO [16]. For completeness, we restate the assumptions, methods, and key findings of this earlier effort, which were first presented at the 9th Annual Space Traffic Management Conference of the International Academy of Astronautics (IAA STM 2023), in this paper. In addition, we relax the zero-phase-angle assumption previously made and explore the effect of Sun-RSO-CST phase angle on useful RSO-CST detection range. We also investigate a number of CST sensor characteristics not previously considered, including aperture diameter, pixel pitch, focal length, and optical field of view (FOV), and describe the constraints they may impose on the feasibility of using CSTs to detect and track RSOs. The methodology for these analyses is described in Sec. 2, with key findings reported and discussed in Sec. 3. Conclusions and recommendations for further work are presented in Sec. 4.

Before introducing the theory and methodology for on-orbit debris detection using CSTs, we briefly discuss some alternative sensor systems that have been proposed and even used for space-based SSA. For example, several commercial organizations have explored using radio frequency sensors for SSA applications [4]. However, this approach is not especially useful for detecting debris, which (generally) does not generate radio frequency emissions [4].

In contrast to optical sensors, which generally only provide measurements of angles like azimuth and elevation between the observer and its adequately illuminated target [8], radar systems generally offer measurements of target-observer range and range-rate and can operate independently of target illumination conditions [17]. In order for a radar target to be detected by an observer, the radar emissions must return to the observer after reflecting off their target. As a result, the received signal-to-noise ratio decays with $R^4$, where $R$ is target-observer range [18]. That is, an RSO at a given distance from its observer effectively offers a signal strength *sixteen* times smaller than an identical RSO at half that distance.

Accordingly, there has only been limited work on space-based radar systems for SSA [4]. Nevertheless, Cerutti-Maori et al. [18] developed a concept for a space-based radar system to detect sub-centimeter-scale debris particles. The proposed concept for a 50-W radar system that met their specifications could detect decimeter-scale debris at target-observer ranges approximately as large as 5 km and centimeter-scale debris at ranges approximately as large as 1.6 km [18]. However, our recent work [16] demonstrates that both microsatellite-class CSTs (e.g., [19]) and nanosatellite-class CSTs (e.g., [20]) are capable of detecting debris particles of these size classes at larger target-observer ranges for less than 10% of the power. Although there may be a use-case for space-based radar systems with regards to debris particles smaller than 1 cm in characteristic length, for particles between 1 cm and 10 cm in characteristic length, CSTs offer a more promising solution—especially with the potential for opportunistic, distributed space surveillance at scale.

As a potential hybrid solution, laser ranging systems combine the sensitivity and resolution of optical sensors with the range information and illumination independence characteristic of radar systems [21]. However, space-based debris laser ranging is a relatively new field of research [4], and, much like radar, the strength of the reflected and received signal decays with $R^4$ for targets with characteristic length smaller than the laser beam width [21]. Moreover, laser ranging systems used for debris detection are typically paired with coarser optical systems, which perform the initial scan to inform the laser's fine pointing direction [22], [23]. Thus, a future space-based architecture for SSA using laser ranging systems would likely still rely on CSTs (or similar proliferated optical systems) for on-orbit debris detection at scale.

## 2. Theory and Methodology

This section summarizes the mathematical and physical relationships used to generate the results discussed in Sec. 3 and Appendix A. We first present a mathematical relationship for the AVM of a near-Earth RSO as a function of its optical properties and distance from the observer before presenting a table of representative CSTs and a selection of properties relevant to the overall discussion. We then relax the zero-phase-angle assumption and explore the effects of angular resolution and streak speed, defined in Sec. 2.5, on detection feasibility.

### *2.1. Apparent Visual Magnitude for Near-Earth Debris*

The ability of a CST to observe an RSO is a function of that RSO's AVM, as viewed by the satellite observer. According to McGraw et al. [24] (as cited by Driedger and Ferguson [25]), for RSOs in LEO, this parameter, $V_{\rm rso}$, can be defined in terms of the AVM of the Sun at Earth, $V_{\rm sun}$, the distance from the RSO to the observing CST, $R$, and the object's optical cross section (OCS), $A_{\rm opt}$:

$$V_{\rm rso} = V_{\rm sun} - \frac{5}{2}\log_{10}\frac{A_{\rm opt}}{R^2} \tag{1}$$

Eq. 1 is reverse logarithmic, such that brighter objects have more negative AVM values. In this equation, the AVM of the Sun at Earth is given by $V_{\rm sun} = -26.5$ [25].

In general, $A_{\rm opt}$ is a time-dependent function of the RSO's geometry, material properties, and angle relative to the Sun and observer. For larger RSOs that can be detected using ground-based optical sensors, if the RSO-sensor distance is known, Eq. 1 can be used to derive an average value for $A_{\rm opt}$ using time-averaged, ground-based AVM measurements [25], [26]. Table 1 presents these mean OCS estimates—along with associated inputs to Eq. 1—for three select spacecraft. Of particular note is the 10-cm-diameter, spherical POPACS spacecraft, which serves as a useful baseline against which to compare corresponding data for 10-cm debris particles [26].

The information in Table 1, in accordance with the methodology used by Driedger and Ferguson [25], uses orbital altitude as the RSO-sensor distance input to Eq. 1. A more rigorous approach would account for the normalized ranges used by Gasdia [26], but the overall conclusions are the same using either approach for the purposes of the present analysis.

For smaller RSOs and debris, however, a different approach is required to eliminate this time dependency and simplify optical debris analysis campaigns. To this end, the Inter-Agency Space Debris Coordination Committee (IADC) has established a standard in which each orbital debris particle is modeled as a diffuse Lambertian sphere with a phase angle—that is, the Sun-debris-observer or the Sun-RSO-CST angle—of $\phi = 0°$ and a surface reflectivity or albedo of $\rho = 10\%$ [27]. The Barker (2004) model (attributed to Barker et al. [28] by Hostetler and Cowardin [29]) for optical measurements of sunlit near-Earth RSOs leverages this Lambertian sphere simplification in its function for the OCS of a debris particle in LEO [27]:

$$A_{\rm opt} = \frac{1}{4}\pi d^2 \rho F(\phi) \tag{2}$$

where, in addition to the already-defined parameters, $d$ represents the diameter of the Lambertian sphere, and $F(\phi)$ is the phase function for the given phase angle, which, according to Williams and McCue [30], is given by:

$$F(\phi) = \frac{2}{3\pi^2}[(\pi - \phi)\cos(\phi) + \sin(\phi)] \tag{3}$$

Combining Eqs. 1–3 yields a useful relationship for the AVM of a Lambertian debris particle with known size, reflectivity, phase angle with respect to the Sun and observer, and distance from the observer:

$$V_{\rm rso} = V_{\rm sun} - \frac{5}{2}\log_{10}\frac{\frac{1}{4}\pi d^2 \rho F(\phi)}{R^2} \tag{4}$$

It is worth noting that Eqs. 2–4 do not assign any particular value for surface reflectivity or phase angle. However, for the IADC standard model of $\rho = 10\%$ and $\phi = 0°$, the phase function becomes:

$$F(0) = \frac{2}{3\pi} \tag{5}$$

and Eq. 4 simplifies to:

$$V_{\rm rso} = V_{\rm sun} - \frac{5}{2}\log_{10}\frac{d^2}{60R^2} \tag{6}$$

Eq. 6 is used, under the standard IADC assumptions, to visualize AVM as a function of RSO-CST distance and debris size in Sec. 3.1, Sec. 3.2, and Appendix A. Eq. 4, on the other hand, is used to explore the relationship between phase angle and RSO-CST detection range in Sec. 2.3 and Sec. 3.3, in which the zero-phase-angle assumption is relaxed.

Table 1: Mean OCS values for select spacecraft, adapted from [25] and [26] as stated.

| Spacecraft | Char. Length (cm) | Mean Orbit Alt. (km) | Sun AVM | Mean AVM | Mean OCS ($m^2$/sr) |
|---|---|---|---|---|---|
| POPACS NanoSat [26] | 10 | 838 | $-26.5$ | 12 | 0.00028 |
| SpinSat [25] | 56 | 345 | $-26.5$ | 9 | 0.00075 |
| DMSP-5D2 F7 [25] | 930 | 835 | $-26.5$ | 7 | 0.02776 |

### 2.2. *Representative CSTs and Selected Properties*

Zakharov et al. [31] have investigated several different classes of star tracker (ST) and tabulated a variety of parameters for assessing and comparing the respective performance of each imager. Of particular note is the AVM cutoff value, $V_{\rm cutoff}$, which represents the dimmest AVM that can be detected by a ST for a given signal-to-noise ratio (SNR) and exposure time, $\tau$. Table 2 presents these three quantities and other relevant parameters for three representative ST classes [31]. The front-illuminated (FI) CST can be considered to represent the class of ST that could be found on a typical microsatellite, whereas the high-precision (HP) CST would represent a comparatively high-end optical sensor, likely custom developed in a laboratory environment, and the nano CST class corresponds to those STs that could be found on low-budget, space-constrained CubeSats and other nanosatellites.

Since Zakharov et al. [31] assume square image detector frames and square pixels, Table 2 captures the pixel pitch, $p$, which represents the center-to-center distance between the pixels of the detector array [33], as a single parameter, rather than recording two separate and distinct dimensions. Likewise, the size of the detector array is also represented by a single parameter, $M$, corresponding to the number of pixels on one side of the square detector, and the corresponding FOV along one side of the detector is represented by $\psi$. The total number of pixels in the detector can be determined by taking the product $M \times M$, and the corresponding square FOV is given by the product $\psi \times \psi$. Other parameters presented in Table 2 include the focal length, $f$, and the aperture diameter, $D$, of the imager, which is assumed to have a circular aperture.

Due to continuous improvements in ST and imaging technology, it is likely that the latest generation of CSTs will outperform those imagers investigated by Zakharov et al. [31], so the information presented in Table 2 can be viewed as conservative.

### 2.3. *Phase Angle and Normalized RSO-CST Range*

The zero-phase-angle assumption built into the IADC standard model is most applicable when both the observer and the target RSO pass over the solar terminator while the CST is pointed away from the Sun. Although useful for initial feasibility assessments, this assumption ultimately limits the usefulness of leveraging CSTs to detect and track debris in LEO by restricting this strategy to a fairly niche operating regime. Relaxing the zero-phase-angle assumption would address this issue and, consequently, increase the generality of the proposed strategy.

Thus, we seek to understand the effect of phase angle on RSO-CST detection range. To begin, we express $R$, the RSO-CST range from Eq. 4, as an explicit function of the phase function, $F(\phi)$. That is,

$$R \equiv R[F(\phi)] \tag{7}$$

Solving Eq. 4 for $R[F(\phi)]$ yields:

$$R[F(\phi)] = \left[\frac{1}{4}\pi d^2 \rho * 10^{-\frac{2}{5}(V_{\rm sun} - V_{\rm rso})} * F(\phi)\right]^{\frac{1}{2}} \tag{8}$$

As discussed in Sec. 2.2, the dimmest AVM that can be detected by a given CST is given by its $V_{\rm cutoff}$ value. To isolate the effect of phase angle on detection capability, we set $V_{\rm rso}$ in Eq. 8 above equal to $V_{\rm cutoff}$, as follows:

$$V_{\rm rso} \equiv V_{\rm cutoff} \tag{9}$$

The relationships in Eq. 8 and Eq. 9 are used to explore detection range as a function of phase angle in Sec. 3.3 for each of the three representative imagers presented in Table 2.

Moreover, for any debris particle modeled as a Lambertian sphere such that $\rho$ and $d$ are fixed, for a given CST with known AVM cutoff value, we can claim that:

$$\left[\frac{1}{4}\pi d^2 \rho * 10^{-\frac{2}{5}(V_{\rm sun} - V_{\rm cutoff})}\right]^{\frac{1}{2}} = \text{constant} \tag{10}$$

Under these conditions, RSO-CST detection range is proportional to the square root of the phase function and is, therefore, ultimately a function of phase angle alone, as shown in Eq. 11:

$$R[F(\phi)] \propto [F(\phi)]^{\frac{1}{2}} \tag{11}$$

This enables the normalization of RSO-CST detection range as a function of phase angle with respect to the corresponding (maximum) detection range associated with a phase angle of $\phi = 0°$:

$$\frac{R[F(\phi)]}{R[F(0)]} = \left[\frac{F(\phi)}{F(0)}\right]^{\frac{1}{2}} \tag{12}$$

This relationship, which is agnostic to debris size, surface reflectivity, sensor sensitivity, and even the brightness of the Sun, is discussed further in Sec. 3.3.

Table 2: Selected properties of representative CSTs/imagers, adapted from [31] unless otherwise stated.

| CST Type | Example | $\tau$ (s) | $f$ (cm) | $p$ ($\mu$m) | $M$ | $D$ (cm) | $\psi$ (°) | SNR (dB) | $V_{\mathbf{cutoff}}$ |
|---|---|---|---|---|---|---|---|---|---|
| HP CST/Imager | MOST [32] | 0.1 | 50 | 12 | 1024 | 6.70 | 1.41 | 11 | 11.1 |
| FI CST | BOKZ-MF | 0.1 | 4 | 16 | 512 | 1.88 | 11.69 | 15 | 6.5 |
| Nano CST | BST ST200 | 0.1 | 2 | 20 | 256 | 0.98 | 14.59 | 7 | 4.8 |

### *2.4. Angular and Spatial Resolution*

The presence of millions of RSOs in LEO and the fact that CSTs can observe multiple RSOs in a single image presents the realistic possibility that two RSOs may be so close to one another in a given snapshot that they appear to the imager as indistinguishable [15]. Since distinguishing and uniquely identifying the RSOs observed will be essential for improving the state of the art in tracking of LEO RSOs via space-based sensors, it is useful to quantify this effect and the extent to which it reduces the parameter space for CST-based debris detection. The ability of an optical imager to distinguish two point sources of light—e.g., two LEO RSOs—from one another is quantified by its *angular resolution* [33], [34]. In the absence of atmospheric effects, lens aberrations, and other camera defects, the optimal angular resolution of an optical system is determined by the more restrictive of two limiting factors [35]. The first of these, the *diffraction limit*, is associated with the physical phenomenon of diffraction, in which light naturally bends as it passes around an obstacle or through an opening, such as the aperture of a CST [34], [36]. In order for an optical system to resolve information at its diffraction limit, its image detector must be able to support such precise angular resolution. In practice, however, the angular resolution of a real space-based optical system may be governed by its *detector limit*—that is, the FOV of its detector pixels [33], [34]. In particular, two RSOs imaged by the same pixel would appear to the sensor as a single source of light, rather than two resolved entities [33], [34]. For ground-based optical imagers, angular resolution is often limited by atmospheric distortions, rather than diffraction or detector limits, but space-based imagers can theoretically operate at their respective governing limit if there are no lens aberrations or other camera defects [35]. Assuming the absence of these imperfections, discussed briefly in Sec. 3.6, most space-based optical systems are capable of producing images with angular resolution at or approaching the more restrictive of these theoretical limits and are often described as being diffraction limited or detector limited, respectively [35].

For optical imagers with circular apertures, such as those presented in Table 2, the diffraction-limited angular resolution is given by the *Rayleigh criterion*, $\theta_{\mathrm{R}}$, which is expressed as a function of light wavelength, $\lambda$, and aperture diameter, $D$, as follows [37], [38]:

$$\theta_{\mathrm{R}} = \arcsin\left(1.2197\frac{\lambda}{D}\right) \tag{13}$$

To translate this angular metric into a more intutive linear metric, we must first introduce the concept of *projected space resolution distance* (PSRD), which is depicted in Fig. 1.

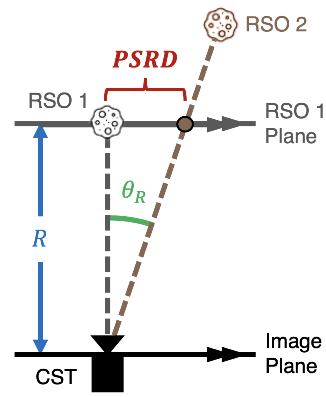


Fig. 1: Geometric definition of PSRD, with $\theta_{\mathrm{R}}$ as Rayleigh criterion and $R$ as RSO-CST range.

In Fig. 1, the second RSO is projected into a plane that intersects the first RSO and is parallel to the image plane of the CST. PSRD represents the in-plane distance between the first RSO and the projection of the second RSO for which the angle between the two is given by $\theta_{\mathrm{R}}$. This is analogous to the concept of ground resolution distance (GRD), which is used in Earth observation applications to denote the distance by which two targets at ground level (e.g., 500 km below a space-based imager) must be separated in order for the imager to resolve them as distinct features [35]. From geometry, the PSRD of a CST with angular resolution $\theta_{\mathrm{R}}$ observing two RSOs at a distance $R$ from the observer is given, under the small angle approximation, by Eq. 14:

$$\mathrm{PSRD} \approx \mathrm{R} * \theta_{\mathrm{R}} \tag{14}$$

The RSO-CST range used in Eq. 14 can correspond to either of the two RSOs without loss of generality. It is worth noting that the Rayleigh criterion is nominally defined for sources of equal strength—in this case, equal AVM [38]. Thus, a more rigorous investigation into diffraction-limited angular resolution involving two RSOs of substantially different AVM is recommended as future work. It is also worth noting that calculations for GRD often consider distortions due to geometric projections and the curvature of the Earth, which reduce the overall resolution capability of the imager [35]. However, in the case of PSRD, if the RSOs are treated as point sources of light, the comparatively simple relationship in Eq. 14 should hold true.

The investigation into detector limits requires a different set of optical properties than is used for diffraction limits. In particular, each image captured by an optical sensor is composed of $M \times M$ pixels, each of which captures a small—but ultimately finite—region of the projected RSO plane first introduced in Fig. 1 [33]. For a square detector with (small) square pixels, this form of angular resolution can be represented by the pixel FOV, $\theta_\mathrm{p}$, depicted in Fig. 2.

Under the small angle approximation, the pixel FOV can be computed from the pixel pitch, $p$, and the imager focal length, $f$, as follows [33]:

$$\theta_\mathrm{p} \approx \arctan\left(\frac{p}{f}\right) \tag{15}$$

As with diffraction-limited angular resolution, it is useful to translate this angular metric into a linear one. Fig. 2 therefore introduces the concept of *projected space sample distance* (PSSD).

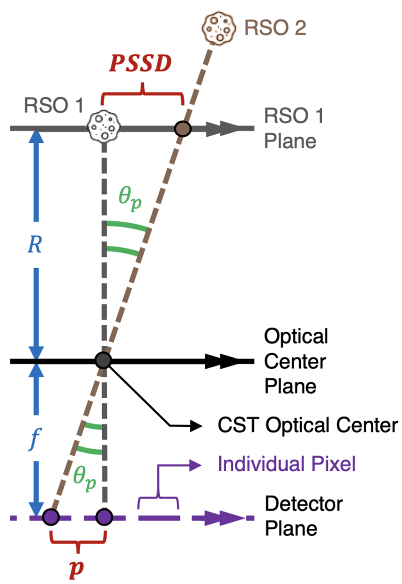


Fig. 2: Geometric definition of PSSD, with $\theta_\mathrm{p}$ as pixel FOV, $f$ as imager focal length, $p$ as pixel pitch, and $R$ as RSO-CST range.

As before, the second RSO is projected into a plane that intersects the first RSO and is parallel to the image plane of the CST. PSSD represents the in-plane distance between the first RSO and the projection of the second RSO for which the angle between the two is given by $\theta_\mathrm{p}$. That is, PSSD corresponds to the minimum RSO-RSO separation, as measured in the RSO plane, for which the imager could resolve the two distinct RSOs in two different pixels. The corresponding equation for PSSD is analogous to the earlier equation for PSRD, with $R$ once again representing the RSO-CST distance:

$$\mathrm{PSSD} \approx \mathrm{R} * \theta_\mathrm{p} \tag{16}$$

PSSD is analogous to the concept of ground sample distance (GSD), which, like GRD, is used in Earth observation applications to describe the size of a projected "ground pixel" captured by a single pixel in a space-based imager [33], [34].

Eq. 13, Eq. 14, and Eq. 16 are all explored graphically in Sec. 3.4 for each of the three represented imagers from Table 2.

### 2.5. *Streak Speed and Field of View*

To complement the previous research efforts investigating relative RSO-CST distances for which the observer could successfully detect the target, this section presents the theory and equations for investigating the relative RSO-CST *speeds* for which detection is feasible. One particular concern is *streaking*, which, in astrophotography, refers to the phenomenon by which point sources of light appear as lines or streaks in the resulting image [13]. This tends to happen when the target object is moving with a high *streak speed*, or speed relative to the observer in a direction perpendicular to the axis of the imager (i.e., projected into the image plane), while the image is being taken. This is depicted geometrically in Fig. 3.

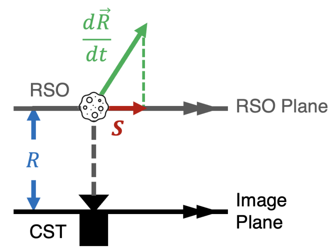


Fig. 3: Geometric definition of streak speed, $S$, with $R$ as RSO-CST range.

A number of strategies have been developed for modeling the light curves from streaks and generating associated RSO position and velocity estimates; however, if the streak speed of the RSO is high enough that the streak spans the entire image and no starting or ending point of the streak can be identified, then position and velocity estimates cannot be generated or are unreliable [11], [13], [14], [15]. A conservative estimate for the maximum allowable streak speed, $S_\mathrm{max}$, can therefore be determined from geometric relations.

For the time scales under consideration (on the order of $\tau = 0.1$ seconds), it is reasonable to use linearized dynamics and assume a (momentarily) fixed inertial orientation for the observer spacecraft [35]. Likewise, although the information presented in Table 2 assumes "square" FOVs associated with the square detector arrays [31], the true projection of the FOV onto the spacecraft sky would be slightly larger than is claimed due to the nature of spherical geometry [35]. However, the square FOV parameter captured in Table 2 as $\psi$ offers a lower bound for measuring this projected area, so the results presented in this section can be treated as conservative. This is depicted geometrically in Fig. 4.

Thus, assuming that the target RSO, streaking in a plane at a distance $R$ from the CST, seeks to traverse the entire CST FOV along the shortest possible path over the CST exposure time, $\tau$, Euclidean trigonometry offers the following relationship:

$$2\tan\left(\frac{\psi}{2}\right) = \frac{S_\mathrm{max} * \tau}{R} \tag{17}$$

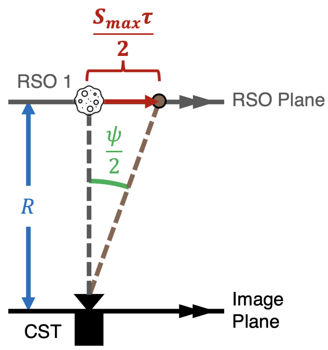


Fig. 4: Geometric definition of maximum detectable streak speed, $S_{\max}$, with $R$ as RSO-CST range, $\tau$ as exposure time, and $\psi$ as sensor FOV along one side of the square frame.

Solving Eq. 17 for the maximum allowable streak speed, $S_{\max}$, yields:

$$S_{\max} = \left[ \frac{2 \tan\left(\frac{\psi}{2}\right)}{\tau} \right] R \tag{18}$$

The effect of FOV and distance on maximum allowable streak speed is explored further in Sec. 3.5.

## 3. Results and Discussion

This section presents the main findings of the analyses discussed in Sec. 2. We begin with a discussion on detection feasibility as a function of RSO-CST distance and RSO characteristic length, assuming zero Sun-RSO-CST phase angle under the IADC standard model. The zero-phase-angle assumption is then relaxed, and the corresponding effects on RSO-CST detection range are discussed. This is followed by graphical representations of angular resolution as a function of CST aperture diameter and PSRD, PSSD, and streak speed as functions of RSO-CST distance for each of the three representative CST types discussed in Sec. 2.2. The section concludes with a discussion of additional—as yet unquantified—limitations, setting the basis for future work.

### *3.1. Detection Feasibility vs. Distance, Parameterized across Debris Size, under Zero Phase Angle*

Under the IADC standard model, the results of Eq. 6, using distance as the input variable, are plotted in Fig. 5 for debris of 1 cm and 10 cm in diameter, in gray and black, respectively. For comparison and to serve as baseline, the results of Eq. 1 for the three spacecraft from Table 1 are also plotted in Fig. 5 as dotted lines. Consistent with Eq. 6, these curves appear as straight lines when plotted on a semi-log scale. In addition, the AVM cutoff value for each imager listed in Table 2 is presented as a horizontal line for reference. Each AVM cutoff line denotes the boundary at which RSOs of a given size and at a given distance can still be detected by the corresponding CST.

From a comparison of the results for 10-cm debris and POPACS, debris roughly 10 cm in diameter appears to be only slightly dimmer than a 10-cm diameter nanosatellite under comparable conditions. This corresponds to an approximate reflectivity coefficient of $\rho = 20\%$ for the nanosatellite, which is consistent with results from prior radiometric studies [39].

From Fig. 5, it is clear that, based on AVM alone, many typical CSTs should be able to detect debris with characteristic length less than 10 cm at distances as far as roughly 50 km when phase angle is zero. These same sensors have the potential to detect debris as small as 1 cm in diameter as far as 5 km away. Even space-limited CubeSats using nanosatellite-class CSTs can detect decimeter-class debris at roughly 25 km away or centimeter-class debris at a distance of 2.5 km. Higher-performing imagers, such as specialized optical telescopes, can further characterize orbital debris of 10-cm diameter as far as 400 km away or be used to characterize orbital debris smaller than 1 cm at ranges not exceeding 40 km.

Brighter and larger objects such as other satellites can be characterized by these CSTs at distances on the order of hundreds or thousands of kilometers, depending on RSO size and reflectivity, as evidenced by the intersections of the solid AVM cutoff lines with the dotted lines corresponding to the three satellites from Table 1.

For completion, an extension of Fig. 5 featuring a broader range of RSO sizes and reflectivity values is presented in Appendix A, Fig. 13.

### *3.2. Detection Feasibility vs. Debris Diameter, Parameterized across Distance, under Zero Phase Angle*

Under the IADC standard model, the results of Eq. 6, using debris diameter as the input variable, are plotted in Fig. 6 across three different RSO-CST ranges (1 km, 10 km, and 100 km). As before, the AVM cutoff value for each imager listed in Table 2 is also shown as a horizontal line denoting the boundary at which an RSO of a given size and at a given distance can still be detected by the corresponding imager. Dotted vertical lines indicate the sizes for SpinSat (56 cm) and POPACS (10 cm). DMSP-5D2 F7 (930 cm) does not appear in Fig. 6 for scaling reasons. It is worth noting that increasing the RSO-CST range by an order of magnitude increases (i.e., makes dimmer) the AVM of a particular debris particle by 5 units, which is consistent with expectations from Eq. 6. This is comparable to the difference between the AVM cutoff values for the HP CST and the FI CST, suggesting that high-performance imagers can generally detect debris an order of magnitude farther away than more typical CSTs.

The intersections of the horizontal AVM cutoff lines in Fig. 6 with the thick range lines offer insights into the smallest debris particle that can theoretically be detected by each imaging sensor at a given range. In broad terms, the results indicate that all three CST classes depicted should be able to detect debris as small as 1 cm at the relatively close range of 1 km and debris larger than 42.5 cm at the relatively far distance of 100 km.

In principle, based on AVM alone, HP CSTs are able to detect debris of diameter as small as 2.5 cm at distances as far as 100 km, and debris smaller than 1 cm in diameter at closer distances. The more typical FI CSTs can detect debris of diameter as small as 2.0 cm at distances as far as 10 km, while nanosatellite-class CSTs can detect 4.0-cm debris at the same distance.

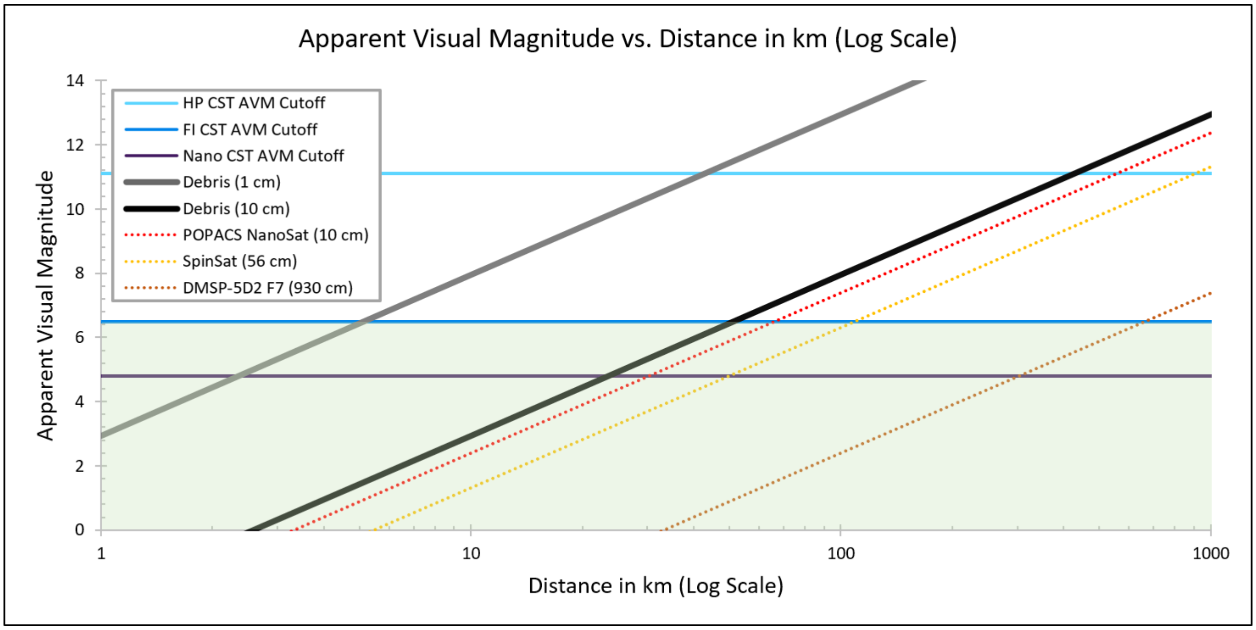


Fig. 5: AVM vs. distance between RSO and CST for representative RSOs of different characteristic length, assuming zero phase angle in accordance with IADC standards [27]. The thin horizontal lines correspond to various sensor AVM cutoffs, while the shaded green region represents the regime which can be detected by typical CSTs. Dotted lines for SpinSat and DMSP-5D2 F7 (adapted from [25]) and for POPACS (using data from [26]) are shown for comparison.

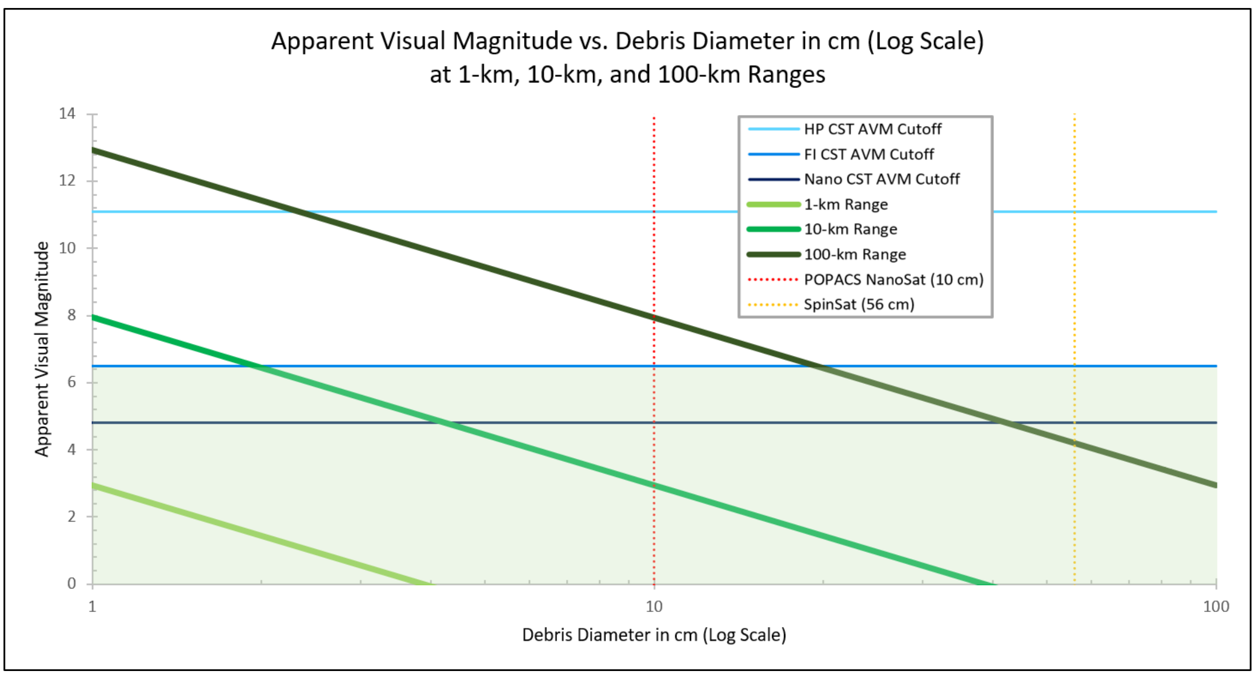


Fig. 6: AVM vs. debris diameter for various RSO-CST ranges, assuming zero phase angle and diffuse Lambertian spheres in accordance with IADC standards [27]. The thin horizontal lines correspond to various sensor AVM cutoffs, while the shaded green region represents the regime which can be detected by typical CSTs. Vertical dotted lines for SpinSat (adapted from [25]) and for POPACS (using data from [26]) are shown for comparison.

As with Sec. 3.1, these results assume zero Sun-RSO-CST phase angle and the absence of other factors that may limit the effectiveness of space-based optical imagers in detecting and tracking RSOs. In the subsections to follow, these findings will be qualified in consideration of phase angle, various sensor properties, and streak speed.

### *3.3. Effect of Phase Angle on RSO-CST Detection Range*

In this subsection, we identify the effect of phase angle on the maximum distance at which each class of optical imager presented in Table 2 can detect a diffuse Lambertian sphere debris particle with 10% reflectivity and characteristic length of 10 cm. For interested readers, a variety of values for reflectivity and characteristic length can be explored using the methodology discussed in Sec. 2.3.

To begin, Fig. 7 offers a graphical visualization of Eq. 8, with $V_{\mathrm{rso}}$ set to the corresponding $V_{\mathrm{cutoff}}$ of each representative CST, in turn, to generate each of the three curves.

As predicted by Eq. 12, the three curves have similar shapes but different zero-phase-angle ranges. In fact, we find that the detection ranges corresponding to $\phi = 0°$ are consistent with the results presented in Sec. 3.1. Namely, the higher-performing imagers are able to detect 10-cm debris particles with 10% reflectivity over 400 km away. For microsatellite-class and nanosatellite-class CSTs, the capability reduces to roughly 50 km and roughly 25 km, respectively. Likewise, although this is not shown in Fig. 7, reducing the debris size to 1 cm reduces the above detection ranges by an order of magnitude, as expected.

As the phase angle grows, the associated detection range decreases—slowly at first before beginning to fall more rapidly after approximately 90°. Nevertheless, the slow initial loss of performance is an attractive result—although phase angle clearly affects detection range and capability, spacecraft are not limited to operation at the solar terminator in order to detect and track LEO RSOs using CSTs.

Fig. 8 shows the normalized detection range metric as a function of the phase angle in degrees. Since Eq. 12 is agnostic to individual CST parameters, only one curve is required.

These data indicate that space-based imagers can be expected to maintain at least 80% of their zero-phase-angle detection range at phase angles as high as 57°. Beyond 90°, however, the performance falls below 57% and rapidly descends thereafter. Regardless, these findings significantly increase the operating envelope for which CST-based RSO detection and tracking will be useful.

### *3.4. Effects of Sensor Properties on Resolution*

In accordance with Eq. 13, the diffraction-limited angular resolution of an optical imager with a circular aperture, as measured by the Rayleigh criterion, is a function of light wavelength and aperture diameter. Most CSTs operate in the range of light wavelengths corresponding to visible light, or approximately 380 nm to 740 nm [40], [41]. For simplicity, this analysis assumes a light wavelength corresponding to the average of these two visible light extremes—560 nm—which roughly corresponds to yellow-green visible light [40].

Thus, Fig. 9 depicts the Rayleigh criterion, computed from Eq. 13, as a function of CST aperture diameter for 560-nm-wavelength light, with dashed vertical lines indicating aperture diameter for the three representative CSTs.

From the intersection of each of the dashed vertical lines with the green angular resolution curve, we can determine the diffraction-limited angular resolution associated with each of the three representative CSTs from Table 2. In descending (i.e., improving) order, the nano, micro, and HP CSTs offer angular resolutions of 14.4 arcsec, 7.5 arcsec, and 2.1 arcsec, respectively. As expected from Eq. 13, for small angles, a two-fold increase in aperture diameter yields an approximately two-fold improvement in angular resolution. In particular, a 0.9-cm increase in aperture diameter from the nano CST to the micro CST results in a 92% (6.9-arcsec) improvement in angular resolution. However, a further 5.4-arcsec improvement in resolution from the micro to the HP CST requires a 256% increase in aperture diameter. Any meaningful improvement beyond this point would require a significant increase to the size of the instrument or else a shift to a higher-frequency electromagnetic wavelength.

Although not explicitly shown in Fig. 9, the results are fairly sensitive to choice of wavelength, and selecting longer or shorter wavelengths worsens or improves, respectively, the diffraction-limited angular resolution of each imager proportionally (for small angles). In fact, recent research has investigated custom STs that operate at infrared wavelengths [41]. For example, for imagers operating at 1550 nm, if aperture diameter is unchanged, the diffraction-limited angular resolution of each CST would worsen by a factor of 2.8. Once again, interested readers are encouraged to explore a variety of values for wavelength and aperture diameter using the methodology discussed in Sec. 2.4.

Since linear distances are more intuitive than angular resolutions, Fig. 10 takes the angular resolutions from Fig. 9 and applies them to Eq. 14 to generate three individual curves for PSRD vs. RSO-CST range. Due to the small angle approximation, the relationship is essentially linear in all three cases. A horizontal dashed red line is also present to indicate a benchmark RSO-RSO separation value of 10 m, which is comparable to the accuracy at a range of 1000 km of certain ground-based optical telescopes used by the U.S. SSN [42].

These results indicate that, for all three CSTs, the diffraction-limited angular resolutions from Fig. 9 correspond to PSRDs less than 10 m for RSO-CST ranges as far as 100 km. In particular, the PSRD of the high-precision imager is approximately 10 m for an RSO-CST range of 1000 km. In other words, the HP CST can resolve two RSOs of comparable AVM 1000 km away as long as they are at least 10 m apart. For comparison, the angular resolution of the tracking and imaging radar operated by the FGAN research institute in Germany is approximately 0.0002°, which corresponds to a PSRD of about 3.5 m at a range of 1000 km [43]. Similarly, the angular accuracy of optical telescopes used by the U.S. SSN can be as high as 5 arcsec, which corresponds to a PSRD of about 24 m at a range of 1000 km [42]. Given that the performance of the HP CST in this regard is roughly comparable to the performance of ground-based space surveillance systems, diffraction-limited angular resolution is not expected to be a significant limiting factor in the performance of CST-based RSO characterization [42].

Likewise, Fig. 11 depicts the results for PSSD vs. RSO-CST range from Eq. 16. We find that, for all three representative imagers from Table 2, PSSD is

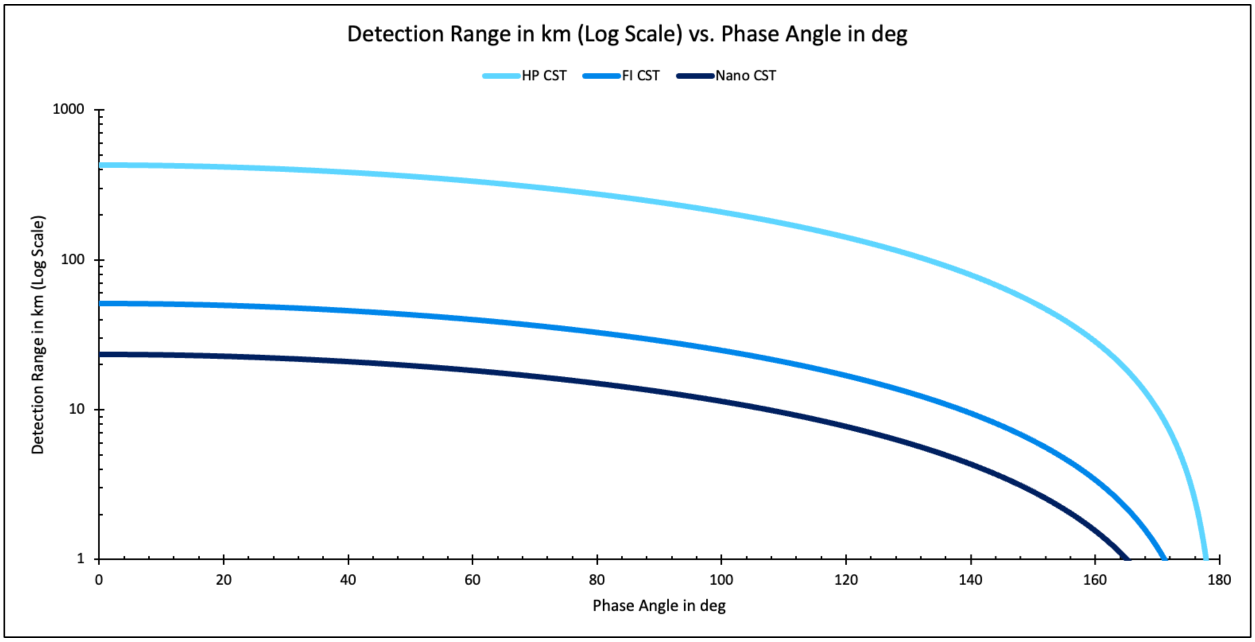


Fig. 7: RSO-CST detection range vs. phase angle for each of the three representative CST classes, using parameters from Table 2, assuming 10-cm debris particles and diffuse Lambertian spheres with 10% reflectivity in accordance with IADC standards [27].

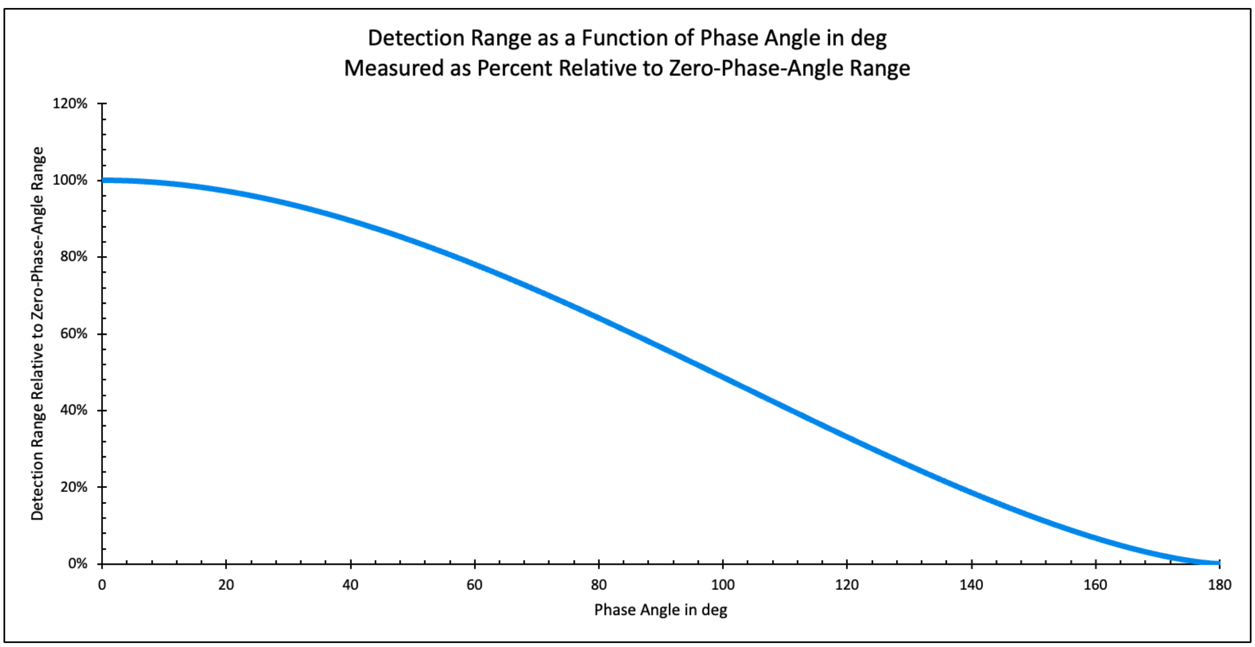


Fig. 8: Normalized RSO-CST detection range—expressed as a percentage of the corresponding detection range at zero phase angle—vs. phase angle, assuming diffuse Lambertian spheres in accordance with IADC standards [27].

the more significant limiting factor by approximately an order of magnitude. It is worth noting that this may not be true in general for all imagers, since the results will vary as functions of light wavelength, aperture diameter, focal length, and pixel pitch. However, for the microsatellite-class CST in particular, the benchmark RSO-RSO separation of 10 m is exceeded for RSO-CST ranges beyond approximately 25 km. At a distance of 1000 km, the RSOs must be separated by at least 400 m, as measured in the RSO plane, in order to be captured in two different microsatellite-class CST image pixels. Since these PSSD metrics are roughly an order of magnitude more restrictive than the corresponding PSRD metrics, *detection-limited* angular resolution may serve

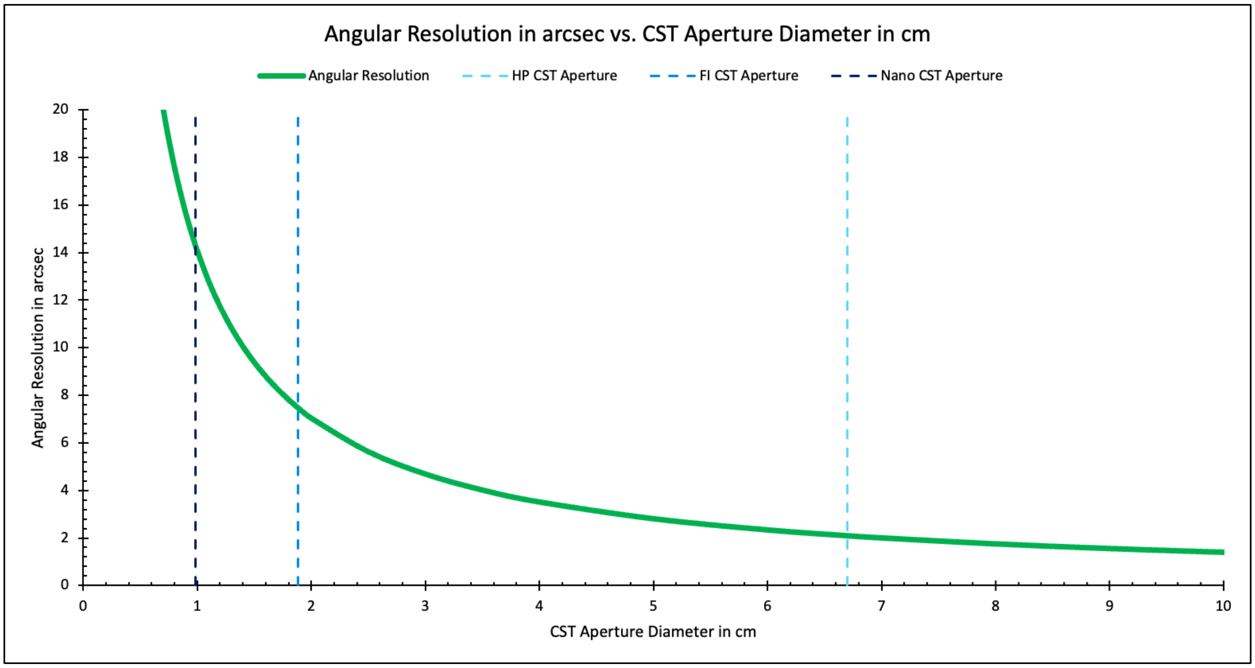


Fig. 9: Angular resolution vs. CST aperture diameter, assuming a visible light wavelength of $\lambda = 560$ nm and circular apertures, with thin vertical lines corresponding to the respective aperture diameters of the three representative CST classes presented in Table 2.

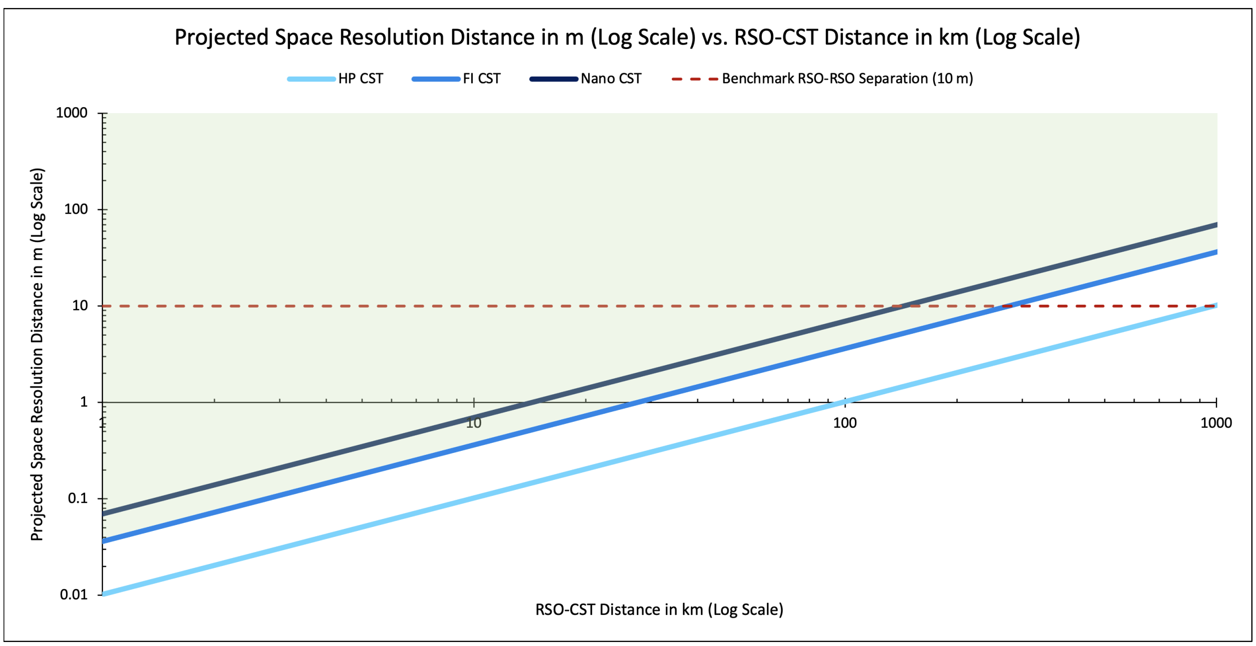


Fig. 10: PSRD vs. RSO-CST range for each of the three representative CST classes, using sensor parameters from Table 2, with shaded green region representing the regime which can be detected by typical microsatellite-class CSTs.

as a meaningful limitation on the usefulness of CST-based RSO detection and should be incorporated into any future simulation work on this topic.

Fig. 10 and Fig. 11 are presented on log-log scales to show a broader range of RSO-CST values along the horizontal axis.

### 3.5. *Effect of Streak Speed on Detection Capability*

It is a well-established fact that RSOs captured in CST images tend to appear as streaks, and recent research has investigated methods for successfully estimating RSO position and velocity from these streaks [11], [13], [14], [15], [44]. The goal of this subsection is to

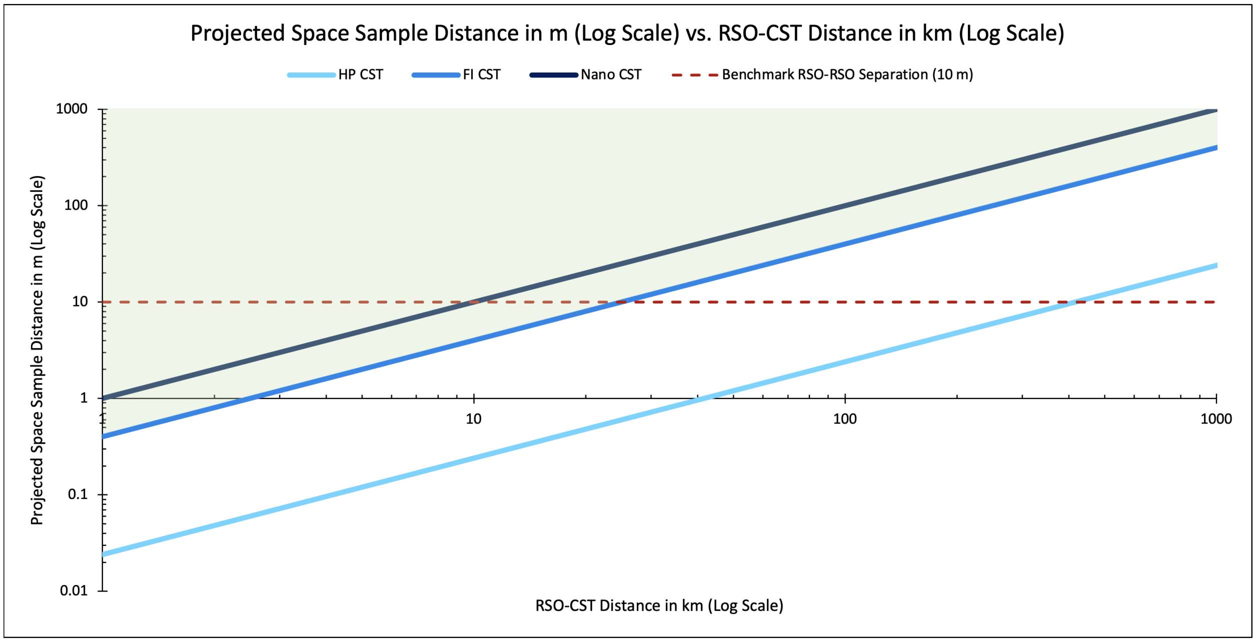


Fig. 11: PSSD vs. RSO-CST range for each of the three representative CST classes, using sensor parameters from Table 2, with shaded green region representing the regime which can be detected by typical microsatellite-class CSTs.

establish a benchmark maximum streak speed for objects in LEO and to investigate and visualize the effect of FOV and RSO-CST range on the maximum streak speed that is allowable in accordance with Eq. 18.

In principle, objects merely visiting LEO may be traveling at arbitrarily high velocities when they are imaged by a CST. However, the majority of LEO RSOs reside in low-eccentricity or near-circular orbits [35], and the fastest theoretical speed that an RSO in a circular Earth orbit can attain is approximately 7.905 km/s, which corresponds to the speed of a satellite orbiting Earth at an altitude of 0 km above ground [35]. To set a reasonable upper bound for streak speed, we consider a situation in which the target RSO and the CST are both (momentarily) moving at this theoretical maximum speed in antiparallel directions at the instant of imaging. In this case, the benchmark maximum streak speed is given by:

$$S_{\mathrm{max,benchmark}} = 2\left(7.905\frac{\mathrm{km}}{\mathrm{s}}\right) = 15.810\frac{\mathrm{km}}{\mathrm{s}} \quad (19)$$

This benchmark represents the maximum streak speed that, in principle, a CST could encounter in its quest to detect LEO RSOs. It is depicted as a horizontal dashed red line in Fig. 12, which uses Eq. 18 to depict maximum detectable streak speed vs. RSO-CST range for each of the three representative CSTs from Table 2.

The intersection of the horizontal dashed red line with each of the diagonal blue lines yields the *minimum* RSO-CST range above which any images taken by that particular CST should include at least one endpoint of the streak of a target LEO RSO. The only exception to this finding would be any LEO RSOs that are streaking at speeds in excess of 15.810 km/s, which, as discussed above, is highly unlikely.

In a deviation from most of the other findings in this paper, the HP CST does *not* outperform the other representative imagers with regards to maximum detectable streak speed. In descending (i.e., improving) order, the HP, micro, and nano CSTs would be able to image the full streak of a LEO RSO traveling at $S_{\mathrm{max,benchmark}}$ at RSO-CST ranges of at least 64.3 km, 7.7 km, and 6.2 km, respectively. Ultimately, given the narrow FOV of the HP CST, this is a logical result and serves as a meaningful limitation on the capability of HP CSTs to detect high-streak-speed objects.

The physics involved in Eq. 18 are largely independent of debris size. However, as discussed in Sec. 3.1, in order to detect smaller debris, the RSO-CST range must generally be reduced to compensate for the reduced AVM of the target RSO. Fig. 12 indicates that, in such cases, the feasible parameter space for debris detection is constrained by maximum detectable streak speed.

For example, in Sec. 3.1, we found that nano CSTs could detect 1-cm debris out to approximately 2.5 km (assuming zero phase angle). From Fig. 12, this corresponds to a maximum detectable streak speed of approximately 6.0 km/s, which is appreciably less than the theoretical maximum benchmark streak speed established in Eq. 19. Thus, at such distances, some RSOs may reasonably be traveling with relative velocities that preclude proper detection by the CST. Combining this result with those of Sec. 3.3, at non-zero phase angles, the maximum detectable RSO-CST range for a given RSO would be reduced further, resulting in lower maximum detectable streak speeds.

For proper investigation of the coupling of these various constraints and their intersectional effects on the feasible parameter space for CST-based RSO detection and tracking, we recommend the development and analysis of detailed simulations as future work.

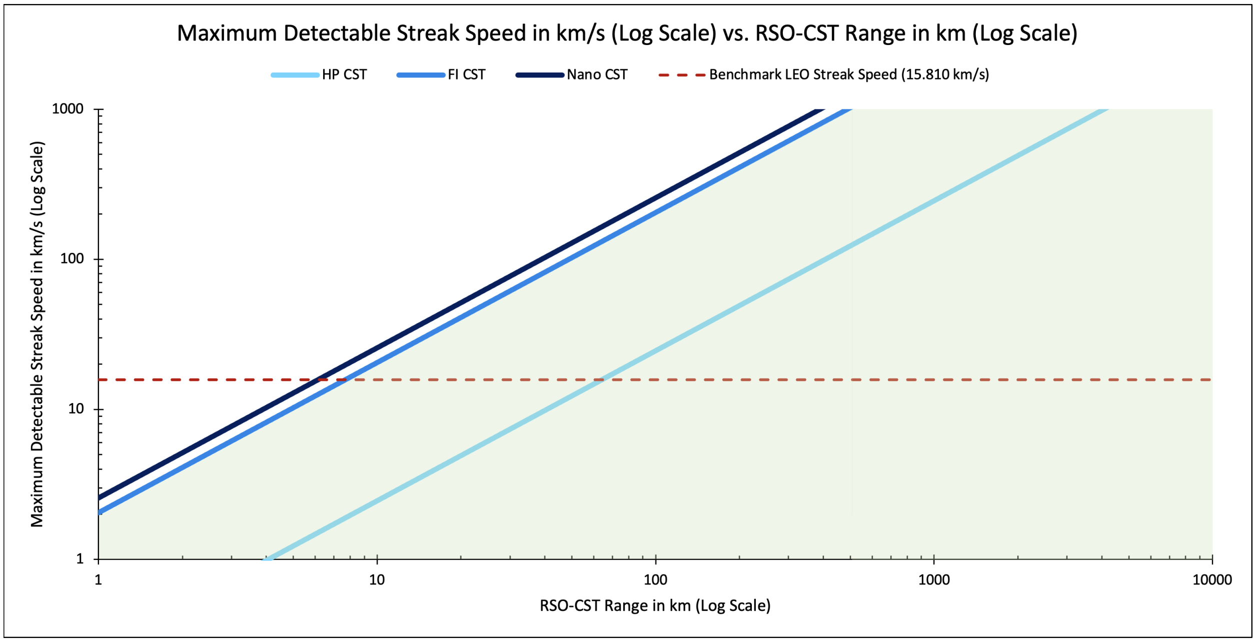


Fig. 12: Maximum detectable streak speed vs. RSO-CST range for each of the three representative CST classes, using sensor parameters from Table 2, assuming square FOVs and detectors, with shaded green region representing the regime which can be detected by typical microsatellite-class CSTs.

### *3.6. Additional Limitations*

Beyond the limiting factors and constraints already discussed in Sec. 2 and Sec. 3, we briefly consider a number of additional qualitative and quantifiable (but as yet unquantified) constraints on CST-based RSO detection performance.

One of the primary qualitative limitations in this regard is not physical but logistical in nature. In particular, an appreciable fraction of CSTs that are currently on orbit do not generally save any images taken during nominal operation; instead, they output attitude information (e.g., quaternions) directly to the spacecraft flight computer, discarding any RSO-related information in the process [19]. Changing this behavior as a whole for all affected on-orbit CSTs would likely require patches to spacecraft software or CST firmware, which is unlikely—if not impossible—without mass collaboration from the aerospace industry. Although it may be possible to bypass any need for saving images by using onboard RSO detection or state estimation algorithms [44], widespread software or firmware patches would be required in any case. However, with enough progress and interest in the field of space-based space surveillance, it may be possible to change this behavior for future space missions.

It has also been hypothesized that simultaneous attitude determination and RSO recognition will burden the computers onboard participating spacecraft [44]. However, researchers have been investigating this issue for several years now and have developed lightweight algorithms for onboard RSO detection with minimal effect on required CST and spacecraft computational power [11], [44].

Furthermore, aberrations in the star tracker lens generally reduce their effectiveness in detecting and tracking illuminated space objects [31]. In particular, chromatic and spherical aberrations, coma, astigmatism, distortion, and curvature of field are some of the principal aberrations that tend to reduce performance in optical systems [35]. Since optical aberration theory is a mature field, quantifying these limitations and their effects on the feasible parameter space for CST-based detection of RSOs is identified as future work [31].

## 4. Conclusions and Future Work

In this paper, we summarized the results of previous research, which indicated that CSTs can be used to detect orbital debris particles between 1 cm and 10 cm in diameter up to specified distances, and expanded on these analyses by investigating additional parameters that may limit the usefulness of CST-based debris detection. In addition to the CST AVM cutoff values investigated previously, we studied non-zero phase angles, pixel pitch, angular resolution, aperture diameter, and FOV. As before, the debris particles were modeled in accordance with IADC standards and treated as diffuse Lambertian spheres with 10% surface reflectivity. The Barker (2004) model [28], defined for optical measurements of sunlit RSOs near Earth, was used to relate the AVM of the RSOs to their characteristic length, phase angle, and distance from the observer. A series of three representative imagers was identified to characterize the effects of their various optical and geometric properties on CST-based RSO detection capability [31]. The traditional zero-phase-angle assumption of the IADC standard model was relaxed in order to investigate the effect of phase angle on RSO-CST detection range. The ability of the selected CSTs to resolve two RSOs in the same image (i.e., angular resolution) and to detect streaking RSOs was likewise investigated to characterize any potential limitations associated with angular (and, by extension, projected linear) resolution and relative RSO-CST velocity. The discussion concluded with a brief consideration of other limiting factors.

The overall results are generally favorable with regards to the use of CSTs to detect space debris. We identify a series of parameters to consider for accurate simulation and assessment of space-based debris detection via CSTs. As discussed in Sec. 3.1 and Sec. 3.2, we find that adequately illuminated sub-decimeter-class debris particles can be detected by typical microsatellite-class CSTs at distances of tens of kilometers when the Sun-RSO-CST phase angle is assumed to be zero. These RSO-CST detection ranges are even greater for larger and brighter RSOs and more sensitive optical imagers. As shown in Fig. 7, relaxing the previous zero-phase-angle assumption only reduces the useful RSO-CST detection range by 20% for phase angles up to 57°. Moreover, we find that the dependence on phase angle is independent of other RSO and CST parameters under consideration when the RSO-CST detection range is normalized by the corresponding zero-phase-angle range.

We likewise find that, for the RSO-CST ranges over which CST-based detection of LEO debris would be useful, diffraction-limited angular resolution is not a significant limiting factor. Moreover, for the three representative CSTs we explored in detail, we find that *detector-limited* angular resolution proved to be approximately an order of magnitude more limiting than its diffraction-limited counterpart and, as such, is worthy of consideration in any future simulation work on this topic. These conclusions were supported by translating the angular results from Eq. 13 and Eq. 15 into more intuitive linear distances represented by PSRD and PSSD values in Fig. 10 and Fig. 11, respectively. In practice, however, for the purposes of a space-based debris detection simulation, it is more efficient to investigate angular resolution than PSRD or PSSD, as the linear figures of merit require additional computational operations relative to their angular counterparts.

The investigation into the relationship between FOV and streak speed revealed additional limitations of CST-based RSO detection capability. For example, smaller FOVs are associated with lower maximum allowable streak speeds, all else being equal. This effect is particularly noticeable for smaller (and dimmer) objects, which can only be detected at comparatively small RSO-CST distances. Ultimately, this does not eliminate the possibility of detection, but it does serve as a useful constraint for any future simulation work that will leverage space-based optical sensors for debris detection. Moreover, a general trend among the three CST classes explored indicates that a higher AVM cutoff correlates with a lower FOV. Thus, although higher-precision CSTs can generally observe smaller debris particles at a given distance, they are limited in the volume of space they can scan and the relative velocity of the RSOs they can detect. More rigorous simulation work is required to assess the overall performance of these HP CSTs relative to the microsatellite- and nanosatellite-class CSTs with regards to improving SSA.

To validate the theoretical findings from our analysis, future work should consider experimenting with a variety of real CST images—acquired from on-orbit spacecraft with known states and sensor properties—that have captured coincident RSOs with known states, geometries, and optical properties. Another promising direction for further study is investigating angular resolution relationships between two RSOs of substantially different AVM, since the Rayleigh criterion definition nominally applies to light sources of equal brightness [38]. In addition, quantifying the effects of optical aberrations and other imager imperfections on RSO-CST detection range and AVM cutoff values would provide additional practical constraints on the usefulness of leveraging CSTs for detecting debris. Finally, now that the feasibility of using CSTs to *detect* sub-decimeter-scale debris particles in LEO has been demonstrated, future work should consider *tracking* such particles using a network of satellites.

## Acknowledgments

This research was sponsored in part by the United States Air Force Research Laboratory and the United States Air Force Artificial Intelligence Accelerator and was accomplished under Cooperative Agreement Number FA8750-19-2-1000. The views and conclusions contained in this document are those of the authors and should not be interpreted as representing the official policies, either expressed or implied, of the United States Air Force or the U.S. Government. The U.S. Government is authorized to reproduce and distribute reprints for Government purposes notwithstanding any copyright notion herein. Allan Shtofenmakher was also supported in part by the Graduate Fellowships for STEM Diversity, the National Institute of Standards and Technology, and the Arthur Gelb (1961) Endowed Fund. The authors would like to thank Sydney Dolan and Victor Qin for technical discussions and feedback.

## Appendix A: Additional Detection Feasibility vs. Distance Curves for a Variety of Representative RSOs

Fig. 13 extends the results of Fig. 5 to a greater variety of RSOs with different optical and geometric properties and to a wider range of RSO-CST distances, extending up to 35,786 km on the rightmost end of the horizontal axis. Under the IADC standard model, the results of Eq. 6, using distance as the input variable, are plotted for debris of 1 cm, 10 cm, and 100 cm in diameter, in dark gray, black, and light gray, respectively. As with Fig. 5 from Sec. 3.1, Fig. 13 features horizontal lines representing the AVM cutoff values for the imagers listed in Table 2, each of which denotes the boundary at which an RSO of a given size and at a given distance can still be detected by the corresponding CST.

In addition, Fig. 13 includes curves for all combinations of representative satellites with characteristic lengths of 10 cm, 100 cm, and 1000 cm and reflectivity values of 20% and 50%. The former reflectivity value is typical of intact satellites, while the latter is among the highest of historically observed satellite albedos [39]. These curves are generated under the zero-phase-angle assumption and the diffuse Lambertian sphere approximation using Eq. 6. It is worth noting that the usefulness of the latter approximation is limited with regards to modeling complex (e.g., non-spherical) satellite shapes, the AVM of which depends on the attitude of the spacecraft and its surfaces and the optical and geometric properties of those surfaces [27].

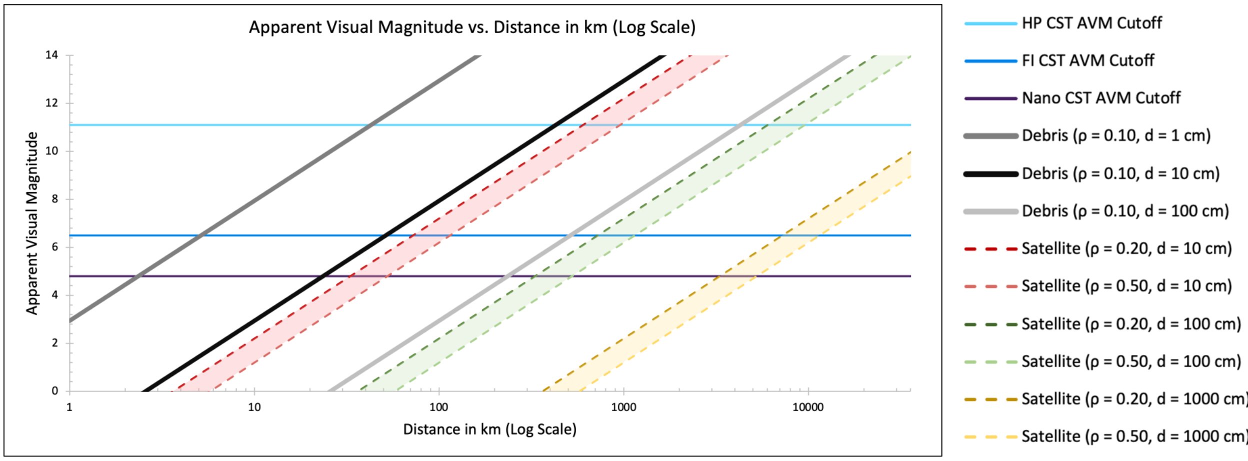


Fig. 13: AVM vs. distance between RSO and CST for a variety of RSO reflectivity values and characteristic lengths, assuming zero phase angle in accordance with IADC standards [27]. The thin horizontal lines correspond to various sensor AVM cutoffs, while each shaded region represents a continuum of reflectivity values between 20% and 50% for satellites with characteristic lengths of 10 cm (red), 100 cm (green), and 1000 cm (yellow), respectively.

Nevertheless, some useful trends are apparent in Fig. 13. In particular, within a given size class (e.g., 10 cm, 100 cm, or 1000 cm), satellites generally appear to be brighter than debris at a given RSO-CST range. Whereas a typical microsatellite-class CST may be able to detect meter-scale debris particles roughly as far as 500 km away, the same imager would be able to detect meter-scale satellites as far as 725 km or even 1150 km away, depending on the reflectivity values of the satellite surfaces. Fig. 13 also suggests that specialized optical sensors like the HP CST have the potential to detect, from LEO, decameter-scale and larger satellites in geosynchronous and geostationary orbits. In contrast, microsatellite- and nanosatellite-class CSTs would likely be limited to LEO-to-LEO SSA operations, where they can still provide substantial benefit with regards to improving awareness of the space domain.

## References

[1] R. Hiles, A. Alexander, N. Herzer, D. McKissock, A. Mitchell, J. Sapinoso, Report on 2020 mega-constellation deployments and impacts to space domain awareness, in: Advanced Maui Optical and Space Surveillance Technologies Conference, Maui, HI, 2021.
URL `https://amostech.com/TechnicalPapers/2021/SSA-SDA/Hiles.pdf`

[2] K. L. Hobbs, A. R. Collins, E. M. Feron, Towards a taxonomy for automatic and autonomous cooperative spacecraft maneuvering in a space traffic management framework, in: AIAA ASCEND, 2020.
URL `https://doi.org/10.2514/6.2020-4240`

[3] B. Weeden, Space situational awareness fact sheet, Online, accessed: 2023-07-20 (May 2017).
URL `https://swfound.org/media/205874/swf_ssa_fact_sheet.pdf`

[4] B. Lal, A. Balakrishnan, B. M. Caldwell, R. S. Buenconsejo, S. A. Carioscia, Global trends in space situational awareness (SSA) and space traffic management (STM), Tech. Rep. D-9074, Log H 18-000179, Institute for Defense Analyses Science and Technology Policy Institute, Washington, DC (April 2018).
URL `https://apps.dtic.mil/sti/pdfs/AD1123106.pdf`

[5] B. Tingley, Russia releases 1st images of damage to leaky Soyuz spacecraft (photos), accessed: 2023-12-15 (February 2023).
URL `https://www.space.com/soyuz-spacecraft-leak-photos-russia-space-agency`

[6] Space Launch Schedule, Soyuz MS-23: Soyuz 2.1a, accessed: 2023-09-14 (February 2023).
URL `https://www.spacelaunchschedule.com/launch/soyuz-2-1a-soyuz-ms-23/`

[7] E. Howell, Russia's 'final decision' on leaky Soyuz spacecraft at space station to come in January: reports, accessed: 2023-12-15 (December 2022).
URL `https://www.space.com/russia-leaky-soyuz-decision-january-2023`

[8] J. Sharma, G. H. Stokes, C. von Braun, G. Zollinger, A. J. Wiseman, Toward operational space-based space surveillance, Lincoln Laboratory Journal 13 (2) (2002) 309–334.
URL `https://archive.ll.mit.edu/publications/journal/pdf/vol13_no2/13_2spacesurveillance.pdf`

[9] Air Force Space Command, Space Based Space Surveillance, Online, accessed: 2023-07-20 (July 2019).
URL `https://www.afspc.af.mil/About-Us/Fact-Sheets/Article/249017/space-based-space-surveillance/`

[10] M. Liu, H. Wang, H. Yi, Y. Xue, D. Wen, F. Wang, Y. Shen, Y. Pan, Space debris detection and positioning technology based on multiple star trackers, Applied Sciences 12 (7) (April 2022).

URL https://doi.org/10.3390/app12073593

[11] S. Dave, R. Clark, G. Chianelli, R. Lee, Machine learning implementation for in-orbit RSO orbit estimation using star tracker cameras, in: Advanced Maui Optical and Space Surveillance Technologies Conference, Maui, HI, 2022.
URL https://amostech.com/TechnicalPapers/2020/Machine-Learning-Applications-of-SSA/Dave.pdf

[12] S. Dave, R. Lee, RSO position and velocity estimation using convolutional neural networks from in-orbit star tracker images, in: 43rd Committee on Space Research Scientific Assembly, 2021.

[13] L. Varela, L. Boucheron, N. Malone, N. Spurlock, Streak detection in wide field of view images using convolutional neural networks (CNNs), in: Advanced Maui Optical and Space Surveillance Technologies Conference, Maui, HI, 2019.
URL https://amostech.com/TechnicalPapers/2019/Machine-Learning-for-SSA-Applications/Varela.pdf

[14] R. Linares, R. Furfaro, Space object classification using deep convolutional neural networks, in: 19th International Conference on Information Fusion, Heidelberg, Germany, 2016.
URL https://ieeexplore.ieee.org/document/7528013

[15] S. Clemens, R. Lee, P. Harrison, W. Soh, Feasibility of using commercial star trackers for on-orbit resident space object detection, in: Advanced Maui Optical and Space Surveillance Technologies Conference, Maui, HI, 2018.
URL https://amostech.com/TechnicalPapers/2018/Space-Based_Assets/Clemens.pdf

[16] A. Shtofenmakher, H. Balakrishnan, Feasibility analysis of on-orbit debris detection using commercial star trackers, in: IAA Space Traffic Management Conference, Austin, TX, 2023.
URL https://web.tresorit.com/l/b2cgc#8T1h86yuZ2SdwScwfc_vtA&viewer=PRWRtmo2rg8agY3sFb9x0QCirmMkiMKV

[17] L. Blanks, Operational scheduling of deep space radars for resident space object surveillance, MS thesis, Massachusetts Institute of Technology, Cambridge, MA (May 2022).
URL https://dspace.mit.edu/bitstream/handle/1721.1/145004/Blanks-lindseyb-sm-orc-2022-thesis.pdf?sequence=1&isAllowed=y

[18] D. Cerutti-Maori, J. Rosebrock, I. O. Maouloud, L. Leushacke, H. Krag, Preliminary concept of a space-based radar for detecting mm-size space debris, in: Proceedings of the 7th European Conference on Space Debris, Darmstadt, Germany, 2017.
URL https://conference.sdo.esoc.esa.int/proceedings/sdc7/paper/691/SDC7-paper691.pdf

[19] D. Sinclair, C. Grant, Star Tracker ST-16RT2 Interface Control Document, Rev. 1.32, Sinclair Interplanetary by Rocket Lab, Toronto, Canada, accessed: 2023-09-14 (April 2021).
URL https://www.rocketlabusa.com/assets/Uploads/RL%20-%20Star%20Tracker%20-%20ICD.pdf

[20] T. Delabie, Sagitta Star Tracker Datasheet, V2.0, arcsec, Kuurne, Belgium, accessed: 2024-04-29 (July 2023).
URL https://www.arcsec.space/web/sites/default/files/2023-07/arcsec%20Sagitta%20star%20tracker%20Datasheet%20V2.0.pdf

[21] D. W. Gast, LIDAR design for space situational awareness, MS thesis, Naval Postgraduate School, Monterey, CA (September 2008).
URL https://apps.dtic.mil/sti/tr/pdf/ADA488685.pdf

[22] B. Li, J. Sang, Z. Zhang, A real-time orbit determination method for smooth transition from optical tracking to laser ranging of debris, Sensors 16 (7) (June 2016).
URL https://doi.org/10.3390/s16070962

[23] X. Liu, J. Qiang, G. Huang, L. Zhang, Z. Zhao, R. Shu, Velocity-based sparse photon clustering for space debris ranging by single-photon LiDAR, IEEE Geoscience and Remote Sensing Letters 21 (March 2024).
URL https://doi.org/10.1109/LGRS.2024.3382151

[24] J. T. McGraw, M. R. Ackermann, P. C. Zimmer, J. B. Martin, Blind search for micro satellites in LEO: Optical signatures and search strategies, in: Advanced Maui Optical and Space Surveillance Technologies Conference, Maui, HI, 2003.

[25] M. Driedger, P. Ferguson, Feasibility study of an orbital navigation filter using resident space object observations, Journal of Guidance, Control, and Dynamics 44 (3) (2020) 622–628.
URL https://doi.org/10.2514/1.G005210

[26] F. Gasdia, Optical tracking and spectral characterization of Cubesats for operational missions, MS thesis, Embry-Riddle Aeronautical University, Daytona Beach, FL (May 2016).
URL https://commons.erau.edu/edt/212

[27] J. Africano, P. Kervin, D. Hall, P. Sydney, J. Ross, T. Payne, S. Gregory, K. Jorgensen, K. Jarvis, T. Parr-Thumm, G. Stansbery, E. Barker, Understanding photometric phase angle corrections, in: Proceedings of the 4th European Conference on Space Debris, Darmstadt, Germany, 2005, pp. 141–146.
URL https://conference.sdo.esoc.esa.int/proceedings/sdc4/paper/108/SDC4-paper108.pdf

[28] E. S. Barker, J. L. Africano, D. T. Hall, K. S. Jarvis, K. Jorgensen, T. L. Parr-Thumm, P. Seitzer, M. J. Matney, E. G. Stansbery, Analysis of working assumptions in the determination of populations

and size distributions of orbital debris from optical measurements, in: Advanced Maui Optical and Space Surveillance Technologies Conference, Maui, HI, 2004, pp. 225–235.

[29] J. Hostetler, H. Cowardin, Experimentally-derived phase function approximations in support of the Orbital Debris Program Office, in: International Orbital Debris Conference, Sugar Land, TX, 2019. URL https://ntrs.nasa.gov/api/citations/20190033905/downloads/20190033905.pdf

[30] J. G. Williams, G. A. McCue, An analysis of satellite optical characteristics data, Planetary and Space Science 14 (9) (1966) 839–847. URL https://doi.org/10.1016/0032-0633(66)90090-0

[31] A. I. Zakharov, M. E. Prokhorov, M. S. Tuchin, A. O. Zhukov, Minimum star tracker specifications required to achieve a given attitude accuracy, Astrophysical Bulletin 68 (4) (2013) 481–493. URL https://doi.org/10.1134/S199034131304010X

[32] S. Rucinksi, K. Carroll, R. Kuschnig, J. Matthews, P. Stibrany, MOST (Microvariability & Oscillations of Stars) Canadian astronomical micro-satellite, Advances in Space Research 31 (2) (2003) 371–373. URL https://doi.org/10.1016/S0273-1177(02)00628-2

[33] G. Verhoeven, Resolving some spatial resolution issues, AARGnews: Newsletter of the Aerial Archaeology Research Group 57 (6) (2018) 25–34. URL https://core.ac.uk/download/pdf/188647129.pdf

[34] A. G. Hayes, P. Corlies, C. Tate, M. Barrington, J. Bell, J. N. Maki, M. Caplinger, M. Ravine, K. M. Kinch, K. Herkenhoff, B. Horgan, J. Johnson, M. Lemmon, G. Paar, M. S. Rice, E. Jensen, T. M. Kubacki, E. Cloutis, R. Deen, B. L. Ehlmann, E. Lakdawalla, R. Sullivan, A. Winhold, A. Parkinson, Z. Bailey, J. van Beek, P. Caballo-Perucha, E. Cisneros, D. Dixon, C. Donaldson, O. B. Jensen, J. Kuik, K. Lapo, A. Magee, M. Merusi, J. Mollerup, N. Scudder, C. Seeger, E. Stanish, M. Starr, M. Thompson, N. Turenne, K. Winchell, Pre-flight calibration of the Mars 2020 rover Mastcam Zoom (Mastcam-Z) multispectral, stereoscopic imager, Space Science Reviews 217 (29) (2021) 1–95. URL https://doi.org/10.1007/s11214-021-00795-x

[35] J. R. Wertz, D. F. Everett, J. J. Puschell, Space Mission Engineering: The New SMAD, Space Technology Library; v. 28, Microcosm Press, Hawthorne, CA, 2011.

[36] C. R. Nave, Diffraction, accessed: 2023-09-14 (May 2018). URL http://hyperphysics.phy-astr.gsu.edu/hbase/phyopt/diffracon.html

[37] C. R. Nave, The Rayleigh criterion, accessed: 2023-09-14 (September 2018). URL http://hyperphysics.phy-astr.gsu.edu/hbase/phyopt/Raylei.html

[38] Lord Rayleigh F.R.S., Investigations in optics, with special reference to the spectroscope, The London, Edinburgh, and Dublin Philosophical Magazine and Journal of Science 8 (49) (1879) 261–274. URL https://doi.org/10.1080/14786447908639684

[39] P. W. Kervin, J. L. Africano, P. F. Sydney, D. Hall, Small satellite characterization technologies applied to orbital debris, Advances in Space Research 35 (7) (2005) 1214–1225. URL https://doi.org/10.1016/j.asr.2004.11.038

[40] D. Malacara, Color Vision and Colorimetry: Theory and Applications, Second Edition, SPIE Press, Bellingham, WA, 2011.

[41] A. J. Swank, SWIR star tracking, Tech. Rep. NASA/TM-20220007061, NASA Glenn Research Center, Cleveland, OH (May 2022). URL https://ntrs.nasa.gov/api/citations/20220007061/downloads/TM-20220007061.pdf

[42] L. Chen, X.-Z. Bai, Y.-G. Liang, K.-B. Li, Orbital Data Applications for Space Objects, Springer Singapore, Singapore, 2016. URL https://doi.org/10.1007/978-981-10-2963-9

[43] J. R. Alarcón, H. Klinkrad, J. Cuesta, F. M. Martinez, Independent orbit determination for collision avoidance, in: Proceedings of the 4th European Conference on Space Debris, Darmstadt, Germany, 2005, pp. 331–336. URL https://conference.sdo.esoc.esa.int/proceedings/sdc4/paper/77/SDC4-paper77.pdf

[44] D. Spiller, E. Magionami, V. Schiattarella, F. Curti, C. Facchinetti, L. Ansalone, A. Tuozzi, On-orbit recognition of resident space objects by using star trackers, Acta Astronautica 177 (2020) 478–496. URL https://doi.org/10.1016/j.actaastro.2020.08.009